The ternary system Al-Ni-Ti Part I: Isothermal section at 900°C; Experimental investigation and thermodynamic calculation

Bertrand Huneau, Peter Rogl, Kejun Zeng, Rainer Schmid-Fetzer, Marcel Bohn, Joseph Bauer

The ternary system Al–Ni–Ti Part I: Isothermal section at 900°C; Experimental investigation and thermodynamic calculation

B. Huneau [a,b,c], P. Rogl [a,*], K. Zeng [b], R. Schmid-Fetzer [b], M. Bohn [d], J. Bauer [c]

[a] *Institut für Physikalische Chemie der Universität Wien, Währingerstrasse 42, A-1090 Wien, Austria*
[b] *AG Elektronische Materialien, Technische Universität Clausthal, Robert Koch Strasse 42, D-38678 Clausthal-Zellerfeld, Germany*
[c] *Laboratoire de Chimie du Solide et Inorganique Moléculaire, UMR CNRS 6511, Université de Rennes I, Avenue du Général Leclerc, F-35042 Rennes Cedex, France*
[d] *UMR CNRS 6538, Centre de la Microsonde Electronique de l'Ouest, IFREMER, F-29263 Plouzané, France*

Phase relations in the ternary system Al–Ni–Ti have been experimentally established for the isothermal section at 900°C for concentrations $0.1 \leqslant x_{Al} \leqslant 0.7$. The investigation is based on X-ray powder diffraction, metallography, SEM and EMPA-techniques on about 40 ternary alloys, prepared by argon-arc or vacuum-electron beam melting of proper elemental powder blends. The existence of four ternary compounds, τ_1 to τ_4, is confirmed, however, in contrast to earlier investigations at significantly different compositions and with different shape of the homogeneity regions. This is particularly true for the phase regions of τ_3-Al_3NiTi_2 with the $MgZn_2$-type structure ranging from $Al_{30}Ni_{28}Ti_{42}$ (composition lowest in Al) to $Al_{50}Ni_{16}Ti_{34}$ (composition richest in Al) and for τ_2-Al_2NiTi. The complex atom site substitution mechanism in τ_3 changing from Ti/Al exchange at Al-poor compositions towards Ni/Al replacement for the Al-rich part was monitored in detail by quantitative X-ray powder diffraction techniques (Rietveld analyses). In contrast to earlier reports, claiming a two-phase region $Ni\{Al_xTi_{1-x}\}_2 + \tau_3$, we observed two closely adjoining three-phase equilibria: α_2-$AlTi_3 + Ni\{Al_xTi_{1-x}\}_2 + \tau_4$-$AlNi_2Ti$ and α_2-$AlTi_3 + \tau_3$-$Al_2NiTi_2 + \tau_4$-$AlNi_2Ti$. The earlier reported "homogeneous phase at $Al_{23}Ni_{26}Ti_{51}$" was shown by high resolution microprobe and X-ray diffraction measurements to be an extremely fine-grained eutectic. The experimental results are in fine agreement with the thermodynamic calculation.

Keywords: A. Aluminides, miscellaneous; A. Titanium aluminides, based on Ti_3Al; A. Laves phases; B. Phase diagram; E. Phase diagram prediction

1. Introduction

With the formation of extremely fine-grained eutectic microstructures, Al–Ni–Ti alloys have recently attracted attention as soldering or brazing materials for nickel-based superalloy devices as well as for TiAl-based structural intermetallics [1]. Crystal structure data and phase diagram data on the Al–Ni–Ti system, however, are still incomplete although a large variety of published information exists. Despite of several attempts [2,3] towards critical assessments of all the data available on Al–Ni–Ti, more recent investigations of the microstructure of Ni-doped α_2-$AlTi_3$/γ-AlTi alloys [4] as well as of the solidification behaviour of the alloy 14.2Al–29Ni–56.8Ti (at%) [5] revealed severe inconsistencies with respect to the observed and hitherto known compounds or phases and their crystallisation behaviour. These inconsistencies finally prompted a detailed reinvestigation of the Al–Ni–Ti ternary. The present report is the first out of a systematic study of phase equilibria and crystal data within the Al–Ti–Ni–N quaternary and presents the phase relations and crystal structures experimentally derived within the 900°C isothermal section Al–Ni–Ti for $0.1 \leqslant x_{Al} \leqslant 0.7$ in comparison with the thermodynamic calculation.

* Corresponding author.
E-mail address: peter.franz.rogl@univie.ac.at (P. Rogl)

2. Experimental

About 40 samples were prepared starting from high purity powders (purity > 99.9 mass%) of Ti (Johnson-Matthey and Co., UK), Ni (Research Chemicals, Princeton, USA) and Al (Alfa, Karlsruhe, Germany). For arc melting the well blended powder mixtures with a total amount of about 3 g were compacted in $\varnothing = 8$ mm steel dies without the use of lubricants. The pellets were out-gassed prior to melting in an arc melter under Ti/Zr-gettered high purity argon atmosphere. Some of the samples (1 g each) were prepared in an Edwards EB1 electron beam melter in a vacuum of 10 mPa, with a low beam intensity in order to prevent excessive formation of vapour, which may in turn lead to explosion of the liquefied alloy. For better homogeneity the samples were remelted twice or thrice and were then subjected to a long term anneal at 900°C for 240 h in evacuated and sealed silica tubes whose internal surface was lined with Mo-foil to protect the sample from attack by the hot quartz walls. After heat treatment in a thermocouple controlled wire wound tube furnace, the alloys were quenched by rapidly submersing the quartz capsules in water.

Lattice parameters and standard deviations were determined by a least squares refinement of room temperature X-ray powder data either obtained from Guinier–Huber photographs employing monochromatic Cu $K_{\alpha 1}$ radiation and germanium as an internal standard ($a_{Ge} = 0.56576$ nm) or from a Siemens D-5000 diffractometer (Cu K_α) using the Win-index program TREOR [6]. Full matrix full profile Rietveld refinements on X-ray intensities, which were recorded from a flat specimen in the D-5000 diffractometer, were carried out with the FULLPROF program [7]. Powderization of the annealed alloys in the WC–Co mortar introduced some degree of cold working rendering diffuse X-ray reflections. In these cases the powders have been shortly stress-annealed at 900°C for 1 h and quenched prior to X-ray exposure.

Microstructure of the annealed alloys was inspected by light optical microscopy (LOM) on smooth surfaces prepared by grinding (SiC-paper) and polishing the resin mounted alloys with diamond pastes of 3 μm grain size followed by oxide polishing suspension. The scanning electron microscopes (SEM) JEOL JSM 6400 and Leitz AMR 1600T were employed for proper identification of phases and precipitates.

Quantitative composition analyses were performed on a Camebax SX50 wavelength dispersive electron microprobe analyser (EMPA) comparing the K_α emissions of the three elements in the alloys with those from elemental standards and applying a deconvolution and PAP correction procedure [8]. The experimental parameters employed were: acceleration voltage of 15 kV, sample current of 15 nA and spectrometer crystals such as PET for Ti K_α, TAP for Al K_α and LiF for the Ni K_α radiation.

3. Binary systems

The binary systems Al–Ni and Ni–Ti were essentially accepted in the version given in Massalski [9] with modification of the solidification behaviour of $AlNi_3$ after Verhoeven [10]. Al–Ti was used in the form presented in [11,12]. For Ni_3Ti a small homogeneous range from 74.5 to 76 at% Ni was allowed in consistency with earlier findings by [13]. Crystallographic data of all phases pertinent to the Al–Ni–Ti boundary systems are listed in Table 1.

4. Results and discussion

4.1. The isothermal section at 900°C

Fig. 1 presents the isothermal section at 900°C as derived from X-ray powder diffraction, LOM and EMPA data on a series of about 40 ternary alloys. Fig. 1 furthermore shows the tie-lines and concentrations evaluated from the EMP analyses with respect to the nominal composition of each alloy. Crystallographic data from X-ray powder diffraction and results of EMPA are summarised in Table 2 for a selection of representative alloys. Phase equilibria in the Al-poor as well as in the Ni-rich region (> 50 at% Ni) of the ternary system are essentially consistent with the data earlier reported by [13]. For the rest of the diagram there are, however, serious differences regarding the location and homogeneity regions of the ternary compounds observed. They are discussed below.

Due to the formation of an extremely fine-grained eutectic at a composition of about $Al_{23}Ni_{26}Ti_{51}$ microprobe data are easily misinterpreted in terms of a "homogeneous phase". Our high resolution SEM-data (see Fig. 2) undoubtedly reveal the multiphase microstructure in fine accordance with X-ray powder diffraction yielding two closely adjoining three-phase equilibria (see Fig. 1): α_2-$AlTi_3$ + $Ni\{Al_xTi_{1-x}\}_2$ + τ_4-$AlNi_2Ti$ and α_2-$AlTi_3$ + τ_3-Al_2NiTi_2 + τ_4-$AlNi_2Ti$ (see Fig. 3). Thus the composition lowest in Al for τ_3-Al_2NiTi_2 is at $Al_{30}Ni_{28}Ti_{42}$ and no two-phase region $Ni\{Al_xTi_{1-x}\}_2$ + τ_3, as given by [13], exists. Furthermore, the extent of the homogeneity regions of τ_2-Al_2NiTi and τ_3 are entirely different from the findings of [13]. In fact our EMP analyses and X-ray Rietveld refinements confirm a banana-like shape for the homogeneity region of the Laves-type τ_3-phase ranging from $Al_{30}Ni_{28}Ti_{42}$ (composition lowest in Al) to $Al_{50}Ni_{16}Ti_{34}$ (composition richest in Al) with a complicated atom site substitution mechanism changing from Ti/Al exchange at Al-poor

Table 1
Crystallographic data for the boundary phases in the Al-Ni-Ti system

Phase	Pearson symbol	Space group	Prototype	Lattice parameters (pm)			Comments	References
				a	*b*	*c*		
(Al)	cF4	$Fm\bar{3}m$	Cu	404.96			< 660.45°C, at 298 K	[9]
(Ni)	cF4	$Fm\bar{3}m$	Cu	352.40			< 1455°C, at 298 K	[9]
(βTi)	cI2	$Im\bar{3}m$	W	330.65			1670–882°C	[9]
(αTi)	hP2	$P6_3/mmc$	Mg	295.06		468.35	< 882°C, at 298 K	[9]
Al_3Ni	oP16	Pnma	CFe_3	661.8	736.8	481.4	< 854°C, 25 at% Ni	[9,16]
Al_3Ni_2	hP5	$P\bar{3}m1$	Ni_2Al_3	403.6		490.0	< 1133°C, 36.8 to 40.5 at% Ni	[9,16]
AlNi	cP2	$Pm\bar{3}m$	ClCs	288.2			< 1638°C, 42 to 69.2 at% Ni	[9,16]
Al_3Ni_5	oC16	Cmmm	Ga_3Pt_5	747.5	672.7	373.2	< 700°C, 64 to 68 at% Ni	[9,16]
$AlNi_3$	cP4	$Pm\bar{3}m$	$AuCu_3$	357.18			< 1372°C, 73 to 76 at% Ni	[10,16]
$AlTi_3$ (α_2)	hP8	$P6_3/mmc$	Ni_3Sn	578.0		464.7	< 1180°C, 22 to 39 at% Al at $Al_{1.12}Ti_{2.28}$	[9,16]
AlTi (γ)	tP4	P4/mmm	AuCu I	398.69		405.39	< 1460°C, 48 to 61.5 at% Al at 61.5 at% Al	[12]
$Al_{1+x}Ti_{1-x}$ (h)	oP4	Pmmm		402.62	396.17	402.62	1445–1424°C, at 63.5 at% Al	[12]
Al_2Ti (h)	oC12	Cmmm	Ga_2Zr	1208.84	394.61	402.95	1433–1214°C, 66 to 67 at% Al	[12]
Al_2Ti (r)	tI24	$I4_1/amd$	Ga_2Hf	396.7		2429.68	< 1216°C, at 66.7 at% Al	[12]
$Al_{11}Ti_5$ (h)	tI16	I4/mmm	Al_3Zr	392.30 to 393.81		1653.49 to 1649.69	1416–1206°C, 68.5 to 70.9 at% Al	[12]
Al_5Ti_2 (h)	tI28	P4/mmm	Al_5Ti_2	390.53		291.96	1215–985°C, 71.4 at% Al	[12]
βAl_3Ti	tI8	I4/mmm	Al_3Ti	384.88		859.82	1387–600°C, 75 at% Al	[12]
αAl_3Ti							< 600°C, 75 at% Al	[9]
	t*32			387.5		3384.0	Super cell $c = 4c_0$	[16]
	t*64			389.2		6664.0	Super cell $c = 8c_0$	
$NiTi_2$	cF96	$Fd\bar{3}m$	$NiTi_2$	1131.93			< 984°C, 33.3 at% Ni	[9,16]
NiTi (h)	cP2	$Pm\bar{3}m$	ClCs	301.0			< 1310°C, 49.5 to 57 at% Ni	[9,16]
NiTi (r)	mP4	$P2_1/m$	NiTi	289.8	410.8 $\beta = 97.78°$	464.6	Low temperature martensite	[16]
Ni_3Ti	hP16	$P6_3/mmc$	Ni_3Ti	510.88		831.87	< 1380°C, 75 at% Ni	[9,16]

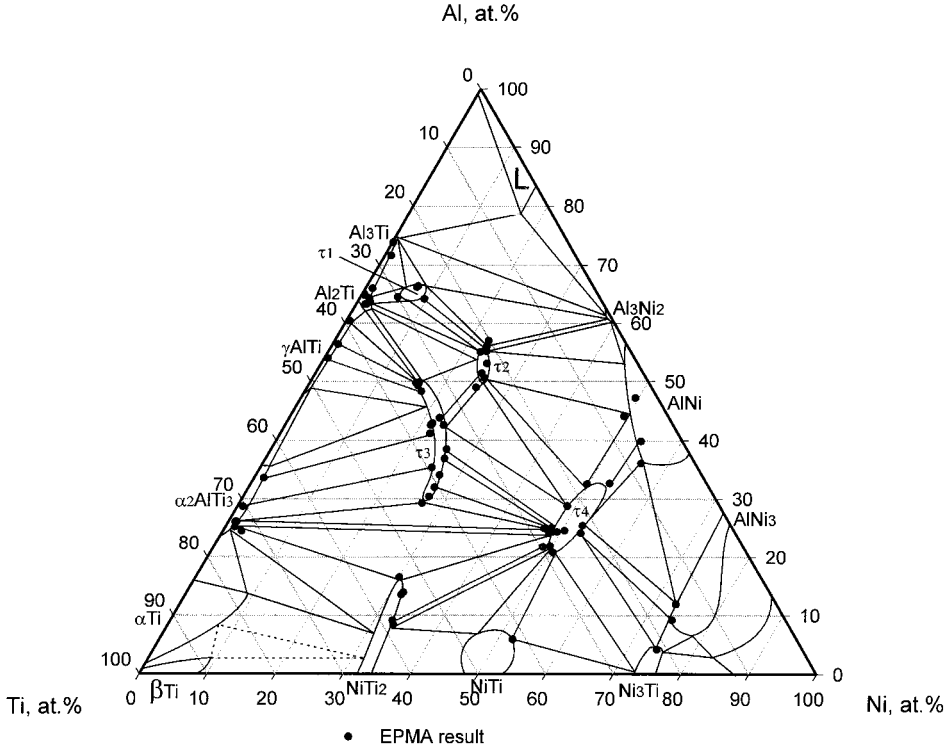

Fig. 1. System Al–Ni–Ti; isothermal section at 900°C for $x_{Al} < 75$ at %. Compositions derived by EMPA are indicated by a small solid dot •.

Table 2
Crystallographic data and results of EMPA of the ternary alloys Al–Ni–Ti

Nominal composition in at%			Phase analysis	Space group	Pearson symbol	Structure type	Lattice parameters (pm)		Volume 10^6pm^3 V	c/a	Results of EMPA (at%)		
Al	Ni	Ti					a	c			Al	Ni	Ti
10.7	33.3	56	$NiTi_2$	$Fd\bar{3}m$	cF96	$NiTi_2$	1127.4 (1)		1432.8 (3)		9.1 (2)	32.7 (2)	58.2 (3)
			$AlNi_2Ti$ (τ4)	$Fm\bar{3}m$	cF16	BiF_3	590.98 (4)		206.40 (3)		21.8 (2)	48.5 (3)	29.6 (2)
			NiTi	$Pm\bar{3}m$	cP2	ClCs	301.2 (2)		27.33 (3)				
14.7	51	34.3	$AlNi_2Ti$ (τ4)	$Fm\bar{3}m$	cF16	BiF_3	590.35 (6)		205.74 (4)		20.8 (3)	50.6 (2)	28.6 (3)
			NiTi	$Pm\bar{3}m$	cP2	ClCs	299.03 (3)		26.74 (5)		5.9 (6)	52.0 (5)	42.0 (3)
			Ni_3Ti	$P6_3/mmc$	hP16	Ni_3Ti	511.07 (4)	833.4 (2)	188.51 (4)	1.6307			
17.1	43	39.9	$NiTi_2$	$Fd\bar{3}m$	cF96	$NiTi_2$	1127.8 (3)		1434.7 (7)		8.4 (1)	33.1 (2)	58.4 (3)
			$AlNi_2Ti$ (τ4)	$Fm\bar{3}m$	cF16	BiF_3	595.02 (7)		206.4 (5)		21.9 (2)	49.6 (3)	28.5 (5)
			NiTi	$Pm\bar{3}m$	cP2	ClCs	300.85 (6)		27.23 (1)				
20	60	20	$AlNi_2Ti$ (τ4)	$Fm\bar{3}m$	cF16	BiF_3	587.80 (7)		203.09 (5)		24.2 (3)	53.0 (5)	22.8 (3)
			Ni_3Ti	$P6_3/mmc$	hP16	Ni_3Ti	510.2 (1)	830.7 (2)	187.22 (8)	1.6282	4.2 (5)	74.3 (1)	21.5 (6)
			Ni_3Al	$Pm\bar{3}m$	cP4	$AuCu_3$	359.54 (5)		46.48 (1)		9.21 (5)	74.0 (3)	16.8 (5)
21	30	49	$NiTi_2$	$Fd\bar{3}m$	cF96	$NiTi_2$	1123.67 (6)		1418.8 (2)		13.9 (3)	31.9 (2)	54.2 (2)
			$AlNi_2Ti$ (τ4)	$Fm\bar{3}m$	cF16	BiF_3	589.99 (5)		205.37 (3)				
			$AlTi_3$	$P6_3/mmc$	hP8	Ni_3Sn	577.0 (3)	467.3 (6)	134.7 (2)	0.8098			
23.3	30.5	46.2	$AlNi_2Ti$ (τ4)	$Fm\bar{3}m$	cF16	BiF_3	589.58		204.95		24.2 (3)	48.3 (3)	27.5 (3)
			$NiTi_2$	$Fd\bar{3}m$	cF96	$NiTi_2$	1122.94		1416.02		13.5 (6)	31.8 (5)	54.7 (6)
			$AlTi_3$	$P6_3/mmc$	hP8	Ni_3Sn					25.2 (5)	1.4 (3)	73.4 (5)
24	20	56	$NiTi_2$	$Fd\bar{3}m$	cF96	$NiTi_2$	1123.67 (8)		1418.8 (2)		16.5 (4)	29.9 (4)	53.5 (6)
			$AlTi_3$	$P6_3/mmc$	hP8	Ni_3Sn	580.03 (5)	466.26 (6)	135.84 (2)	0.8039	24.5 (8)	2.7 (5)	72.8 (4)
			Al_3NiTi_2 (τ3)	$P6_3/mmc$	hP12	$MgZn_2$	502.0 (3)	809.5 (4)	176.6 (2)	1.6125			
25	50	25	$AlNi_2Ti$ (τ4)	$Fm\bar{3}m$	cF16	BiF_3	588.94 (6)		204.28 (4)		24.6 (2)	50.4 (2)	25.0 (2)
			Ni_3Ti	$P6_3/mmc$	hP16	Ni_3Ti	510.9 (2)	833.4 (5)	188.4 (1)	1.6314			
23	10	67	$AlTi_3$	$P6_3/mmc$	hP8	Ni_3Sn	579.71 (5)	465.75 (5)	135.55 (2)	0.8034	26.1 (2)	1.0 (3)	72.9 (3)
			$NiTi_2$	$Fd\bar{3}m$	cF96	$NiTi_2$	1123.3 (2)		1417.4 (3)				
28.8	28.3	42.9	Al_3NiTi_2 (τ3)	$P6_3/mmc$	hP12	$MgZn_2$	501.06	807.18	175.50	1.611	30.4 (2)	27.4 (2)	42.2 (3)
			$AlNi_2Ti$ (τ4)	$Fm\bar{3}m$	cF16	BiF_3	590.21		205.60		25.0 (3)	47.2 (5)	27.8 (5)
			$AlTi_3$	$P6_3/mmc$	hP8	Ni_3Sn	578.94	465.60	135.15	0.804	26.1 (4)	1.2 (4)	72.7 (3)
30.2	59.8	10.0	AlNi	$Pm\bar{3}m$	cP2	ClCs	288.23		23.95		36.1 (2)	55.9 (4)	8.0 (6)
			$AlNi_3$	$Pm\bar{3}m$	cP4	$AuCu_3$	359.18		46.34		11.9 (2)	73.2 (2)	14.9 (1)
			$AlNi_2Ti$ (τ4)	$Fm\bar{3}m$	cF16	BiF_3					25.5	52.6	21.9
33.5	16.6	49.9	Al_3NiTi_2 (τ3)	$P6_3/mmc$	hP12	$MgZn_2$	501.21	810.72	176.37	1.617	35.4 (3)	25.3 (3)	39.3 (3)
			$AlTi_3$	$P6_3/mmc$	hP8	Ni_3Sn	578.41	465.22	13478	0.804	28.6	0.6	70.4
37.8	29.6	32.6	Al_3NiTi_2 (τ3)	$P6_3/mmc$	hP12	$MgZn_2$	499.71	804.84	174.05	1.611	38.5 (2)	25.9 (2)	35.6 (2)
			$AlNi_2Ti$ (τ4)	$Fm\bar{3}m$	cF16	BiF_3	590.79		206.21		25.1 (4)	48.2 (6)	26.7 (4)
38.7	51.4	9.9	AlNi	$Pm\bar{3}m$	cP2	ClCs	289.31		24.22		39.9	53.9	6.1
			$AlNi_2Ti$ (τ4)	$Fm\bar{3}m$	cF16	BiF_3	587.63		202.91		32.7	53.0	14.3
40	12.5	47.5	Al_3NiTi_2 (τ3)	$P6_3/mmc$	hP12	$MgZn_2$	501.2 (1)	810.7 (2)	176.37 (9)	1.6174	41.2 (2)	22.1 (3)	36.7 (3)
			$AlTi_3$	$P6_3/mmc$	hP8	Ni_3Sn	578.4 (1)	465.22 (9)	134.78 (5)	0.8043	33.6 (6)	1.4 (3)	65.1 (7)
43.8	30.6	25.6	Al_2NiTi (τ2)	$Fm\bar{3}m$	cF116	$Mn_{23}Th_6$	1191.28		1690.60		49.0	25.0	26.0
			Al_3NiTi_2 (τ3)	$P6_3/mmc$	hP12	$MgZn_2$	500.12	807.37	174.89	1.614	42.6 (2)	23.4 (2)	34.1 (2)
			$AlNi_2Ti$ (τ4)	$Fm\bar{3}m$	cF16	BiF_3	589.32		204.67		28.8 (9)	48.7 (1)	22.5 (8)
49.5	23.5	27	Al_2NiTi (τ2)	$Fm\bar{3}m$	cF116	$Mn_{23}Th_6$	1190.70 (8)		1688.1 (2)		51.4 (3)	24.6 (3)	24.0 (4)
			Al_3NiTi_2 (τ3)	$P6_3/mmc$	hP12	$MgZn_2$	500.48 (3)	808.2 (1)	175.32 (3)	1.6149	43.8 (5)	22.2 (4)	34.0 (4)
50	37.5	12.5	Al_2NiTi (τ2)	$Pm\bar{3}m$	cF116	$Mn_{23}Th_6$	1189.89 (7)		1684.7 (2)		50.6 (2)	25.4 (3)	24.1 (2)
			AlNi	$Fm\bar{3}m$	cP2	ClCs	289.25 (5)		24.201(8)		47.2 (2)	49.5 (2)	3.3 (2)
			$AlNi_2Ti$ (τ4)	$Fm\bar{3}m$	cF16	BiF_3	588.3 (1)		203.61 (8)				
55	10	35	AlTi	P4/mmm	tP4	AuCu	398.66 (4)	407.68 (9)	64.79 (2)	1.0226	56.4 (4)	0.8 (3)	42.9 (3)
			Al_3NiTi_2 (τ3)	$P6_3/mmc$	hP12	$MgZn_2$					49.7 (2)	15.8 (2)	34.5 (2)
57.6	16	26.4	Al_2NiTi (τ2)	$Fm\bar{3}m$	cF116	$Mn_{23}Th_6$	1191.10		1689.82		55.1 (3)	22.5 (6)	22.4 (4)
			Al_3NiTi_2 (τ3)	$P6_3/mmc$	hP12	$MgZn_2$					49.9 (1)	16.1 (2)	34.0 (2)
			Al_2Ti	$I4_1/amd$	tI24	Ga_2Hf					63.6	1.9	34.5
58.5	7.1	34.4	Al_3NiTi_2 (ττ3)	$P6_3/mmc$	hP12	$MgZn_2$	502.58	823.34	180.10	1.638	49.7 (4)	15.7 (4)	34.6 (2)
			Al_2Ti	$I4_1/amd$	tI24	Ga_2Hf	396.43	2430.32	381.95	6.130	63.3 (2)	1.5 (1)	35.2 (3)
60	18	22	Al_2NiTi (τ2)	$Fm\bar{3}m$	cF116	$Mn_{23}Th_6$	1189.03 (8)		1681.1 (2)		55.1 (3)	23.4 (2)	21.4 (2)
			$Al_{13}Ni_2Ti_5$ (τ1)	$Pm\bar{3}m$	cP4	$AuCu_3$	393.10 (6)		60.74 (2)		64.2 (1)	9.6 (2)	26.1 (2)

(Continued on next page)

Table 2 (*continued*)

Nominal composition in at%			Phase analysis	Space group	Pearson symbol	Structure type	Lattice parameters (pm)		Volume 10^6pm^3 V	c/a	Results of EMPA (at%)		
Al	Ni	Ti					a	c			Al	Ni	Ti
65.0	7.6	27.4	$Al_{13}Ni_2Ti_5$ (τ1)	$Pm\bar{3}m$	cP4	$AuCu_3$	393.71		61.03		64.5 (4)	5.5 (5)	30.0 (6)
			Al_2NiTi (τ2)	$Fm\bar{3}m$	cF116	$Mn_{23}Th_6$	1190.10		1685.58		56.0	23.0	21.0
			Al_2Ti	$I4_1/amd$	tI24	Ga_2Hf					64.3 (3)	1.4 (3)	34.3 (3)
66.1	2.0	31.9	Al_3NiTi_2 (τ3)	$Pm\bar{3}m$	cP4	$AuCu_3$					49.8 (2)	15.7 (2)	34.5 (2)
			Al_2Ti	$I4_1/amd$	tI24	Ga_2Hf	396.489	2429.46	2429.46		63.3 (4)	1.3 (1)	35.4 (4)
			AlTi	P4/mmm	tP4	AuCu					60.4 (4)	0.5 (2)	39.1 (3)
70.3	2.0	27.7	$Al_{13}Ni_2Ti_5$ (τ1)	$Pm\bar{3}m$	cP4	$AuCu_3$	393.90		61.12		66.2 (2)	7.5 (4)	26.3 (3)
			Al_2Ti	$I4_1/amd$	tI24	Ga_2Hf	396.57	2429.08	382.02		64.8 (2)	0.5 (2)	34.7 (2)
			Al_3Ti	I4/mmm	tI8	Al_3Ti					71.7	0.9	27.4
71.7	6.1	22.2	$Al_{13}Ni_2Ti_5$ (τ1)	$Pm\bar{3}m$	cP4	$AuCu_3$	393.58		60.97		66.4 (2)	7.6 (2)	26.0 (1)
			Al_2NiTi (τ2)	$Fm\bar{3}m$	cF116	$Mn_{23}Th_6$	1188.50		1678.82		57.0 (3)	22.8 (2)	20.2 (2)
			Al_2Ti	$I4_1/amd$	tI24	Ga_2Hf					66.0	1.0	33.0
			Al_3Ti	I4/mmm	tI8	Al_3Ti					73.9 (1)	0.1 (1)	26.0 (2)

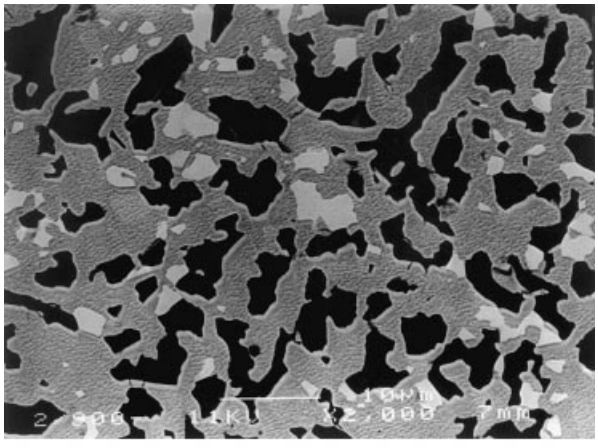

(a)

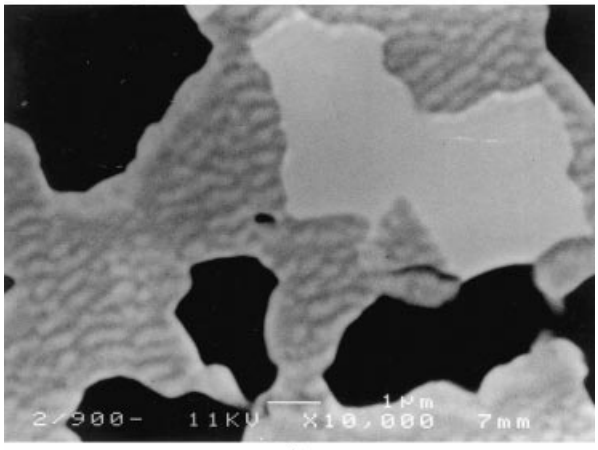

(b)

Fig. 2. Alloy 24Al–20Ni–56Ti (in at%), annealed at 900°C and quenched. (a) SEM, magnification ×10 000: dark particles are α_2-$AlTi_3$ ($Al_{25}Ni_1Ti_{74}$); bright particles are $Ni\{Al_xTi_{1-x}\}_2$ ($Al_{14}Ni_{32}Ti_{54}$), matrix is ultrafine grained eutectic ($Al_{23}Ni_{26}Ti_{51}$); (b) SEM, same alloy with magnification ×2000.

compositions towards Ni/Al exchange for the Al-rich part (for structural details see Section 4.2). The two-phase equilibrium $\tau_3+\tau_4$ as well as the three-phase equilibria $\tau_2+\tau_3+\tau_4$ and $\tau_2+\tau_3+Al_2Ti$ are well documented in the micrographs of Figs. 4–6.

In the Al-rich region we observe the τ_2-phase at a slightly modified location than reported by [13] or [2]. The adjoining three-phase fields: $AlNi+Al_3Ni_2+\tau_2$, $Al_3Ni_2+\tau_2+\tau_1$ ($AuCu_3$-type) and $Al_3Ti+\tau_1+Al_3Ni_2$ are essentially consistent with the phase field distribution reported by [2] for the section at 800°C, although location of the ternary phases and vertices of the three-phase equilibria appear at significantly changed compositions. The two-phase structure $\tau_2+\tau_1$ is revealed in Fig. 7. Whilst a small solid solubility seems to exist for Al_2Ti (dissolving up to 2 at% Ni at 900°C) there is practically no solid solubility for Ni in Al_3Ti and less than 1 at% Ni in γ-AlTi and α_2-$AlTi_3$. We confirm the monotonously increasing solubility of Ti in AlNi raising from 0 at% Ti at $Al_{56}Ni_{44}$ to a maximum of 8 at% Ti at the low Al-side of AlNi ($Al_{36}Ni_{56}Ti_8$). The Ni-poor boundary of $Al\{Ni_{1-x}Ti_x\}_3$ seems to stay constant at 28 at% Ni.

4.2. X-ray diffraction and structural chemistry

4.2.1. Rietveld refinement of the crystal structure of the τ_3-phase with $MgZn_2$-type

The interesting banana-like shape of the homogeneity region of the τ_3-phase ($MgZn_2$-type) suggests already a complex atom site occupation scheme changing from Ti/Al replacement for Al-poor concentrations towards Ni/Al substitution for the compositions richer in aluminium. For further insight into the atom substitution mechanism in order to provide a profound crystallographic basis for a proper thermodynamic description

of the τ_3-phase as a function of composition, we have selected four practically single-phase alloys with various Al-concentrations from the τ_3 homogeneity region for quantitative Rietveld X-ray refinement. The results of these refinements are summarised in Figs. 8 and 9 and Table 3 comprising atom parameters, interatomic distances and residual values. The Rietveld analyses for the alloys: 34.1Al–27.1Ni–38.8Ti, 36.9Al–26.4Ni–36.7Ti, 42.9Al–21.6Ni–35.5Ti and 48.3Al–17.2Ni–34.5Ti (all in at%) in all cases confirmed the crystal symmetry and atom parameters consistent with the $MgZn_2$-type (see Table 3). The variation of the atom parameters and of the interatomic distances as a function of the Al-content merely reflects the usual bonding behaviour in $MgZn_2$-type Laves compounds. It is interesting to note, that the Mg-position (4f site) at the centre of the CN = 16 Laves–Friauf polyhedron seems to be reserved for Ti-atoms and to exclude Al-occupation in τ_3-phase (see Fig. 8). At the Al-poor boundary of the τ_3-phase there is no Ti in

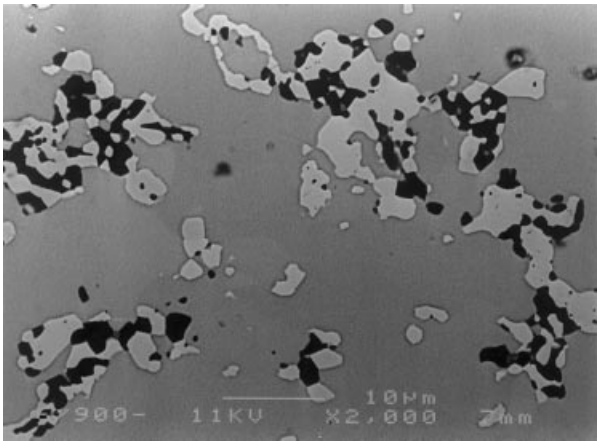

Fig. 3. Alloy 29Al–28Ni–43Ti (in at%), annealed at 900°C and quenched. SEM, magnification ×2000: matrix is τ_3-phase ($Al_{30}Ni_{28}Ti_{42}$); dark phase is $AlTi_3$ ($Al_{26}Ni_1Ti_{73}$); white phase is τ_4-$AlNi_2Ti$ ($Al_{25}Ni_{47}Ti_{28}$).

Fig. 5. Alloy 44Al–30Ni–26Ti (in at%), annealed at 900°C and quenched. SEM image: large dark grey grains are τ_3-phase ($Al_{43}Ni_{23}Ti_{34}$); white phase is τ_4-$AlNi_2Ti$ ($Al_{29}Ni_{49}Ti_{22}$) and dark phase is τ_2-Al_2NiTi ($Al_{49}Ni_{25}Ti_{26}$).

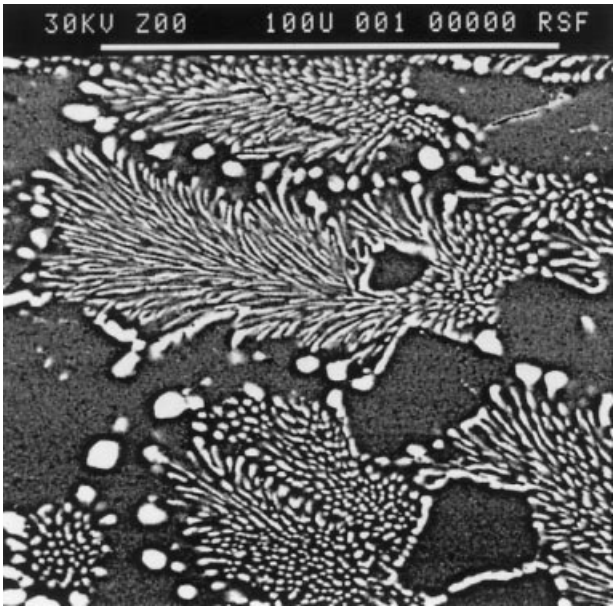

Fig. 4. Alloy 37Al–30Ni–33Ti (in at%), annealed at 900°C and quenched. SEM image: large grains are τ_3-phase ($Al_{38.5}Ni_{26}Ti_{35.5}$); white phase is τ_4-$AlNi_2Ti$ ($Al_{25}Ni_{47}Ti_{23}$).

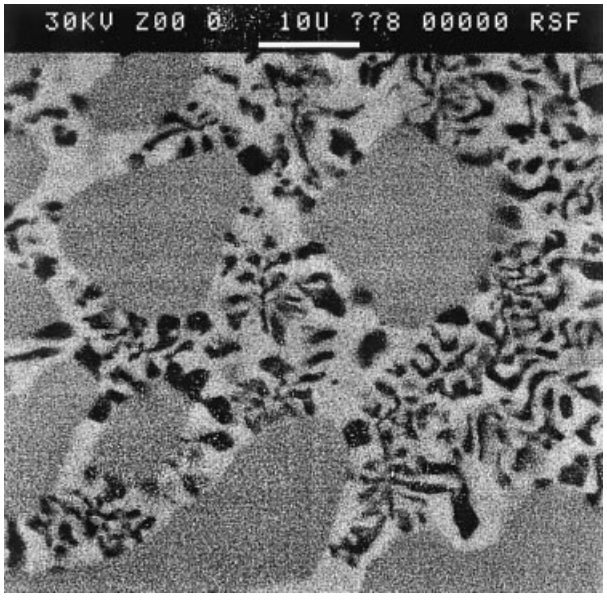

Fig. 6. Alloy 57.5Al–16Ni–26.5Ti (in at%), annealed at 900°C and quenched. SEM image: large grey grains are τ_3-phase ($Al_{50}Ni_{16}Ti_{34}$); light grey phase is τ_2-Al_2NiTi ($Al_{55}Ni_{22.5}Ti_{22.5}$); black particles are Al_2Ti ($Al_{64}Ni_2Ti_{34}$).

the icosahedrally co-ordinated 6h sites. Rising the Al-content of the τ_3-phase results in a gradual substitution of all the titanium by aluminium at the icosahedral centres in 2a, the simultaneous decrease of Ni in 2a and in 6h being compensated by a corresponding increase of Ni in the 4f sites (Fig. 8). For concentrations higher than 40 at% Al, the substitution mode in τ_3 drifts away from a constant Ni-content. With still rising Al-content, Ti-atoms retreat completely from the 2a position but now start to enter the 6h sites. With a thus almost constant Ti-content, aluminium atoms successively replace Ni in the 2a and 6h sites leading at the Al-rich end of τ_3 to practically Ni-free icosahedral centres (2a and 6h) (Fig. 8).

Fig. 9 shows the variation of the unit cell dimensions of the τ_3-phase along its Ni-poor and its Ni-rich phase

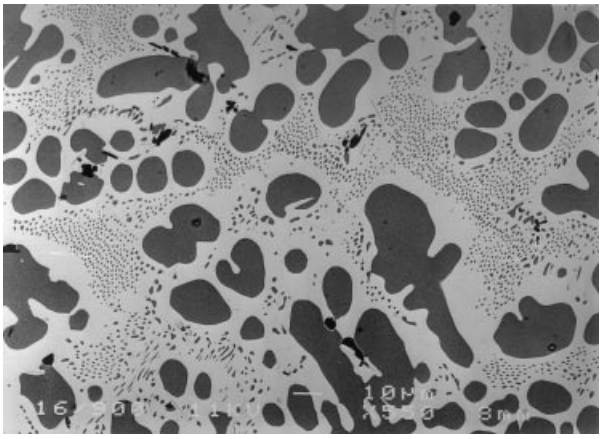

Fig. 7. Alloy 60Al–18Ni–22Ti (in at%), annealed at 900°C and quenched. SEM image, magnification ×550; dark dendrites are τ_1-$Al_{13}Ni_2Ti_5$ ($Al_{64}Ni_{10}Ti_{26}$); white phase is τ_2-Al_2NiTi ($Al_{51}Ni_{25}Ti_{24}$).

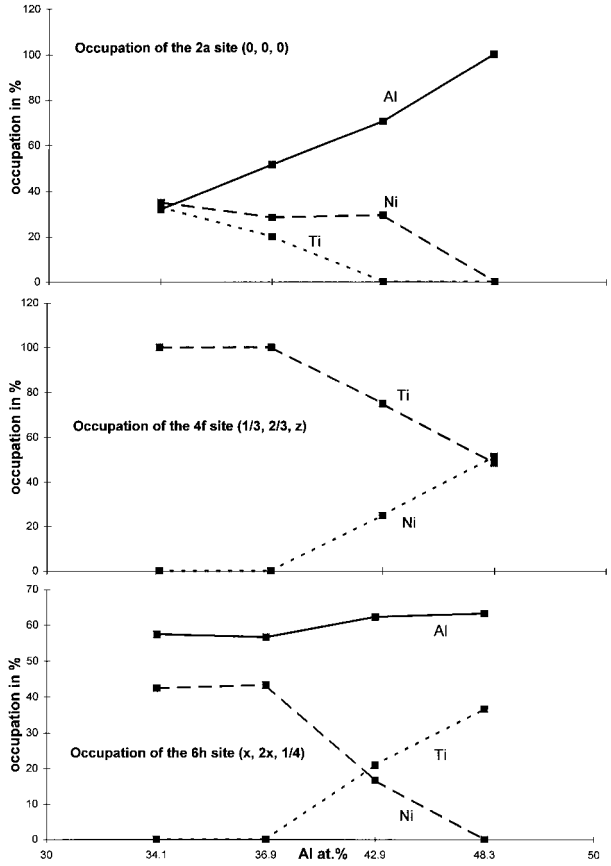

Fig. 8. Occupation of the atomic sites for the τ_3-phase as a function of the Al-content.

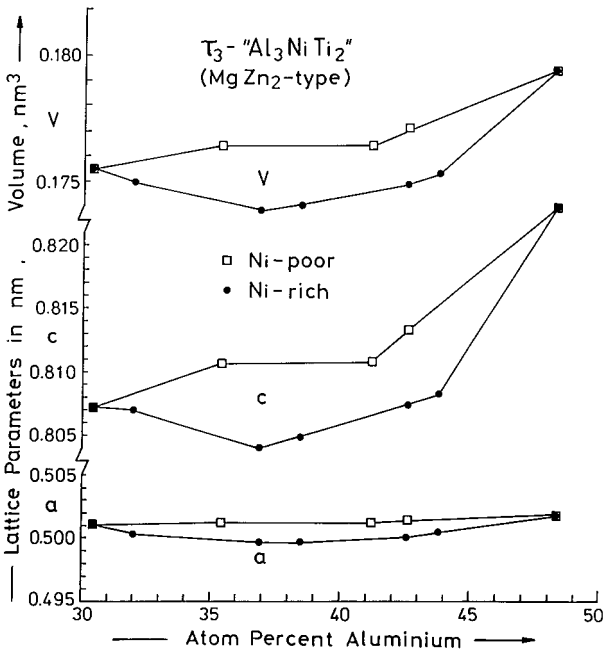

Fig. 9. Variations of the unit cell dimensions of the τ_3-phase along its Ni-poor and Ni-rich region as a function of the Al-content.

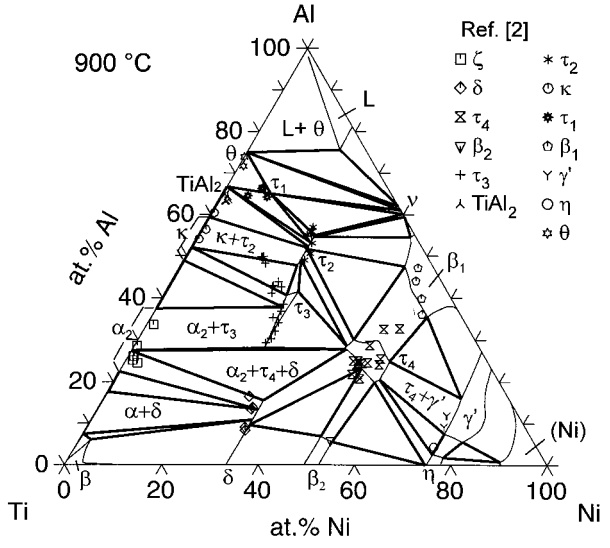

Fig. 10. Calculated isothermal section of the Al–Ni–Ti system at 900°C in comparison with the experimental data from Fig. 1.

boundary as a function of the Al-content. The rather monotonous variation of the unit cell parameters are consistent with the outline of the banana-like homogeneity region of the τ_3-phase in the ternary diagram (see Fig. 1). The appearance of a slight minimum in the Ni-rich unit cell dimensions at around 37 at% Al reflects the complex atom substitution mode shown in Fig. 8 and Table 3. Usually the Laves phases are subdued to a dominant influence of the so-called geometrical factor (radius ratio R_{Mg}/R_{Zn}). With the constraint to form bonding contacts among all near neighbours within the co-ordination shell, extreme radius ratios may lead to strong compression along the Mg–Mg contacts [14]. In agreement with the rather relaxed radius ratio of ≈ 1 for the τ_3-phase we observe closer contacts along the M1–M3 and M3–M3 distances rather than a strong M2–M2 interaction (Table 3). In this respect it is interesting to note, that the τ_3-phase

Table 3
Rietveld refinements for four alloys τ_3-Al_3NiTi_2[a]

Parameter/composition		$Al_{34.1}Ni_{27.1}Ti_{38.8}$	$Al_{36.9}Ni_{26.4}Ti_{36.7}$	$Al_{42.9}Ni_{21.6}Ti_{35.5}$	$Al_{48.3}Ni_{17.2}Ti_{34.5}$
a (nm)		0.50006(2)	0.49956(1)	0.50095(2)	0.50150(1)
c (nm)		0.80446(4)	0.80383(3)	0.81117(3)	0.82249(1)
c/a		1.6087	1.6091	1.6193	1.6440
V [nm^3]		0.1742	0.1737	0.1763	0.1791
Number of variables		18	21	24	14
$R_F = \Sigma\lvert F_o - F_c\rvert/\Sigma F_o$		0.096	0.063	0.087	0.078
$R_I = \Sigma\lvert I_{oB} - I_{cB}\rvert/\Sigma I_{oB}$		0.067	0.077	0.057	0.063
$R_{wP} = \left[\Sigma w_i\lvert y_{oi} - y_{ci}\rvert^2/\Sigma w_i\lvert y_{oi}\rvert^2\right]^{1/2}$		0.145	0.150	0.138	0.138
$R_P = \Sigma\lvert y_{oi} - y_{ci}\rvert/\Sigma\lvert y_{oi}\rvert$		0.113	0.109	0.109	0.104
$R_e = \left\{(N - P + C)/\left(\Sigma w_i\lvert y_{oi}\rvert^2\right)\right\}^{1/2}$		0.062	0.058	0.061	0.061
$\chi^2 = (R_{wP}/R_e)^2$		5.53	6.72	5.04	5.10
Atom parameters					
M1 in 2a (0, 0, 0)		0.64(–)Al	1.03(3)Al	1.41(4)Al	2.00(2)Al
		0.70(1)Ni	0.57(–)Ni	0.59(–)Ni	
		0.66(–)Ti	0.40(–)Ti		
$B_{eq.}(B_{iso})$ 10^2 (nm^2)		3.0(1)	1.5(1)	3.7(1)	2.9(1)
M2 in 4f (1/3, 2/3, z)		4.00(2)Ti	4.00(3)Ti	3.00(5)Ti	1.94(–)Ti
				1.00(–)Ni	2.06(1)Ni
z		0.0572(3)	0.0651(3)	0.06489(3)	0.0681(2)
$B_{eq.}(B_{iso})$ 10^2 (nm^2)		2.87(7)	1.50(7)	3.60(7)	3.04(4)
M3 in 6h (x, $2x$, 1/4)		3.45(5)Al	3.40(6)Al	3.72(1)Al	3.80(3)Al
		2.55(–)Ni	2.60(–)Ni	1.00(–)Ni	2.20(–)Ti
				1.28(–)Ti	
x		0.8295(8)	0.8276(7)	0.8275(8)	0.8294(6)
$B_{eq.}(B_{iso})$ 10^2 (nm^2)		3.02(6)	1.47(6)	3.45(8)	2.99(5)
Distances (nm) within the first nearest neighbor coordination; standard deviations less than 0.0006 nm					
M1	6 M3	0.2495	0.2503	0.2520	0.2535
	6 M2	0.2923	0.2931	0.2940	0.2949
M2	3 M3	0.2845	0.2890	0.2911	0.2974
	6 M3	0.2942	0.2907	0.2921	0.2920
	3 M1	0.2923	0.2931	0.2940	0.2942
	1 M2	0.3102	0.2973	0.3003	0.2992
	3 M2	0.3030	0.3068	0.3078	0.3105
M3	2 M3	0.2443	0.2412	0.2417	0.2448
	2 M1	0.2495	0.2503	0.2520	0.2535
	2 M3	0.2558	0.2584	0.2592	0.2567
	2 M2	0.2845	0.2890	0.2911	0.2974
	4 M2	0.2942	0.2907	0.2921	0.2920
Impurity phases (traces)		Ti_3Al (Ni_3Sn-T)	Ti_3Al (Ni_3Sn-T)	–	Ti_3Al (Ni_3Sn-T)
			$AlNi_2Ti$		$Ti_{22.5}Ni_{24.5}Al_{53}$
			(BiF_3-type)		(Th_6Mn_{23}-type)

[a] Space group $P6_3/mmc$-D^4_{6h} (no. 194); origin at centre, $Z = 2$; $MgZn_2$-type; standard deviations in parentheses. Data collected from flat specimen in D5000; Cu K_α; 2Θ-range from 29 to 110°.

only at high Al-contents is attaining the ideal c/a ratio of 1.63 where the radius ratio turns out to be even smaller than 1 ($R_{M2}/\overline{M}_{1,3} = \frac{1.385}{1.424} = 0.97$). Due to the complex substitution mechanism of the rather differently sized atoms, the ideal atom parameter $x(6h) = \frac{5}{6}$ is reached at high Al-contents, whilst ideal $z(4f) = \frac{1}{16}$ is already found at low Al-contents.

4.2.2. The crystal structure of the τ_2-phase (Th_6Mn_{23}-type)

X-ray powder Guinier data were completely indexed on the basis of a cubic face-centred unit cell. Consistent with the early observations by [15], we note resemblance to a W-type sublattice structure. A Rietveld refinement of the crystal structure of τ_2-Al_2NiTi on the basis of the $Mn_{23}Th_6$-type or the ordered $Cu_{16}Mg_6Si_7$-type as suggested by [16] essentially confirmed crystal symmetry and site occupation with a correspondence as follows: $Cu_{16}Mg_6Si_7$–$(Al,Ti,Ni)_{16}Ti_6(Ni,Al)_7$. With a partial occupation of Al-atoms in an additional site 4b (centre of octahedron; filled Th_6Mn_{23}-type), reliability values can be reached as low as $R_I = 0.06$ (for a detailed analysis see [17]).

4.3. Thermodynamic calculation of phase equilibria (isotherm at 900°C)

Despite the difficulties for a proper thermodynamic description of the various ternary compounds and their partially rather complex atom site occupation schemes, a thermodynamic calculation of the 900°C isothermal section (see Fig. 10) is in fair agreement with the experimental data. It is discussed in detail in the companion paper [18].

Acknowledgements

This work was performed within COST 507-Round II. Financial support by the Austrian Ministry of Science under grant GZ 49.885/2-II/4/93 and by the German BMBF under grant 03K72058 is gratefully acknowledged, as well as by the Training and Mobility (TMR) Programme of the European Commission within the Clausthal Centre of Process Engineering Systems (COPES).

References

[1] Lugscheider E, Schlimbach C, Reinkensmeier I. Experimental investigations in ternary and quaternary Ti–Al–metal systems. Report COST 507, Proc. of the Final Workshop, Vaals, The Netherlands, 9–12 March 1997, Cost Secretariat, Brussels, 1998. p. 90–102.

[2] Budberg PB. The aluminium–nickel–titanium system. In: Petzow G, Effenberg G, editors. Ternary Alloys. Weinheim, Germany: Verlag Chemie, 1993. p. 7–21.

[3] Dupin N. Contribution to the thermodynamic evaluation of multicomponent Ni-based alloys (in French). Thesis, Institut National Polytechnique de Grenoble, 1995. p. 1–259.

[4] Bauer J, Rogl P, Perrin A, Bohn M, Wolf W, Podloucky R, LeFriec Y, Antoine D. TiAl-based alloys with nickel. Intermetallics 1996;4:71–6.

[5] Weitzer F, Rogl P, Hayes F. Unpublished research. UMIST-Manchester, 1996.

[6] Werner PE, Ericson L, Westdahl M. TREOR, a semi-exhaustive trial and error powder indexing program for all symmetries. J Appl Crystallogr 1985;18:367–70.

[7] Rodriguez-Carvajal J. FULLPROF, a program for Rietveld refinement and pattern matching analysis. Abstract of the Satellite Meeting on Powder Diffraction of the XV Congr. Intl. Union of Crystallogr., Toulouse, France, 1990. p. 127.

[8] Pouchou JL, Pichoir F. Electron probe X-ray microanalysis applied to thin surface films and deposits. J Microsc Spectrosc Electron 1985;10:279–305.

[9] Massalski TB. Binary alloy phase diagrams. 2nd edition Materials Park, Ohio: ASM-International, 1990.

[10] Verhoeven JD, Lee JH, Laabs FC, Jones LL. The phase equilibria of Ni_3Al evaluated by directional solidification and diffusion couple experiments. J Phase Equilibria 1991;12(1):15–23.

[11] Schuster JC, Ipser H. Phases and phase relations in the partial system $TiAl_3$–TiAl. Z Metallkunde 1990;81(6):389–96.

[12] Jehn HA. The aluminium–nitrogen–titanium system. In: Petzow G, Effenberg G, editors. Ternary Alloys. Weinheim, Germany: Verlag Chemie, 1993. p. 308.

[13] Nash P, Liang WW. Phase equilibria in the Ni–Al–Ti system at 1173K. Metall Trans A 1985;16A(3):319–22.

[14] Pearson WB. The crystal chemistry and physics of metals and alloys. New York: Wiley-Interscience, 1972.

[15] Raman A, Schubert K. On the crystal structure of some alloy structures related to Ti_3Al. III Investigations in several alloy systems: Ti–Ni–Al and Ti–Cu–Al. Z Metallkunde 1965;56(2):287 (in German).

[16] Villars P, Calvert LD. Pearson's handbook of crystallographic data for intermetallic phases. USA: Materials Park, ASM International, 1991.

[17] Ding JJ, Rogl P, Chevalier B, Weil F. in preparation.

[18] Zeng K, Schmid-Fetzer R, Huneau B, Rogl P, Bauer J. The ternary system Al–Ni–Ti Part II: Thermodynamic assessment and experimental investigation of polythermal phase equilibria. Intermetallics 1999;7(12):1347–1359.